J. Fluid Mech. (2010), *vol.* 658, *pp.* 438–462.
doi:10.1017/S0022112010001825

A deformable liquid drop falling through a quiescent gas at terminal velocity

JAMES Q. FENG†

Cardiovascular R & D, Boston Scientific Corporation, Three Scimed Place C-150, Maple Grove, MN 55311, USA

(Received 25 November 2009; revised 10 April 2010; accepted 10 April 2010; first published online 28 June 2010)

The steady axisymmetric flow internal and external to a deformable viscous liquid drop falling through a quiescent gas under the action of gravity is computed by solving the nonlinear Navier–Stokes equations using a Galerkin finite-element method with a boundary-fitted quadrilateral mesh. Considering typical values of the density and viscosity for common liquids and gases, numerical solutions are first computed for the liquid-to-gas density ratio $\rho = 1000$ and viscosity ratio μ from 50 to 1000. Visually noticeable drop deformation is shown to occur when the Weber number $We \sim 5$. For $\mu \geqslant 100$, drops of Reynolds number $Re < 200$ tend to have a rounded front and flattened or even dimpled rear, whereas those at $Re > 200$ a flattened front and somewhat rounded rear, with that at $Re = 200$ exhibiting an almost fore–aft symmetric shape. As an indicator of drop deformation, the axis ratio (defined as drop width versus height) increases with increasing We and μ, but decreases with increasing Re. By tracking the solution branches around turning points using an arclength continuation algorithm, critical values of We for the 'shape instability' are determined typically within the range of 10 to 20, depending on the value of Re (for $Re \geqslant 100$). The drop shape can change drastically from prolate- to oblate-like when $\mu < 80$ (for $100 \leqslant Re \leqslant 500$). For example, for $\mu = 50$ a drop at $Re \geqslant 200$ exhibits a prolate shape when $We < 10$ and an upside-down button mushroom shape when $We > 10$. The various solutions computed at $\rho = 1000$ with the associated values of drag coefficient and drop shapes are found to be almost invariant at other values of ρ (e.g. from 500 to 1500) as long as the value of ρ/μ^2 is fixed, despite the fact that the internal circulation intensity changes according to the value of μ. The computed values of drag coefficient are shown to agree quite well with an empirical formula for rigid spheres with the radius of the sphere replaced by the radius of the cross-sectional area.

Key words: aerosols/atomization, drops and bubbles, interfacial flows (free surface)

1. Introduction

Under the action of gravity, as in a typical earthbound environment, a liquid drop free from any support surrounded by a quiescent gas will fall at terminal velocity as a result of the balance between its weight and aerodynamic drag. The phenomenon of a liquid drop falling through a quiescent gas occurs frequently in both our everyday life and industrial processes. Yet our understanding of such a basic fluid

† Email address for correspondence: james.feng@bsci.com

mechanical phenomenon has been quite limited, especially for drops with considerable deformations when inertial effect in the relative surrounding gas flow becomes dominant. Ideally, mathematical solutions satisfying the Navier–Stokes equations (based on Newton's second law of motion) and continuity equation (from the principle of conservation of mass) with appropriately specified boundary conditions can provide all the detailed descriptions of fluid mechanics for fundamental understanding. But the nonlinearities arising from fluid inertia and unknown shape of deformable free surface have limited closed-form analytical solutions for a fluid drop moving in another fluid to only extreme situations, such as inviscid or highly viscous fluids and with nearly spherical drop shapes (e.g. Taylor & Acrivos 1964; Harper 1972; Brignell 1973).

The advent of modern high-performance computers has enabled the development of various numerical methods for 'self-consistently' solving complicated nonlinear free-boundary problems such as a fluid drop moving in another fluid. In the published literature, perhaps the first extensive study of the buoyancy-driven motion of a deformable fluid drop through a quiescent fluid was performed by Dandy & Leal (1989) with a finite-difference method using a boundary-fitted orthogonal curvilinear coordinate grid-generation technique (although a preliminary finite-element computational work was presented earlier by Tsukada *et al.* (1984) with a few solutions for cases of small density ratios). Among a wide range of parameters, Dandy & Leal (1989) mostly focused on fluid systems of small density ratio (e.g. 0.91) and viscosity ratio (e.g. 1.33, 2.5, 4), with only very brief illustrations for cases of large density and viscosity ratios comparable to that of typical liquid drops in gases (e.g. a common liquid has a density about 10^3 times and a viscosity of the order of 10^2 times of that of a typical gas under normal conditions). The work of Dandy & Leal (1989) on a liquid drop moving in another fluid was later extended by Helenbrook & Edwards (2002) with more numerical results using a spectral/hp finite-element method for density ratios $\leqslant 500$ and viscosity ratios $\leqslant 15$. Three distinct drop shapes (namely, prolate, oblate and dimpled) were identified, and conditions for forming these shapes were determined (cf. Helenbrook & Edwards 2002). Being interested mainly in transient heat transfer from evaporating droplets, however, Haywood, Renksizbulut & Raithby (1994*a*,*b*) computed deformed droplets at intermediate Reynolds numbers (from 10 to 100) using a finite-volume type of numerical method, and then Hase & Weigand (2004) presented transient three-dimensional results at higher Reynolds numbers (360, 520 and 853) using a volume-of-fluid computational method, but both of them showed few details on drop shape and flow structure.

In this paper, attention is focused on the fluid mechanics of deformable drops with large liquid-to-gas density ratio ($\sim$1000) and large liquid-to-gas viscosity ratio ($\sim$100) moving in another immiscible fluid, as is typical for a liquid drop falling through a quiescent gas. Numerical solutions are computed using a Galerkin finite-element method with full Newton iterations for simultaneously solving the steady axisymmetric Navier–Stokes equations together with the elliptic mesh-generation equations. Because the free-fluid interface coincides with a finite-element mesh line and the grid nodes can move according to the interface deformation, the computational method with a boundary-fitted mesh has been considered to offer the highest accuracy for the present type of problem (as noted by Tryggvason *et al.* 2001). Following the description of mathematical problem and solution method in § 2, the computational results are presented in § 3 for a variety of drop shapes with associated flow structures and values of the drag coefficient. Based on the present findings, practical implications of the computed steady axisymmetric results are discussed in § 4.

2. Mathematical formulation and solution method

The problem under consideration here is a liquid drop of volume $4\pi R^3/3$, constant density ρ_l, viscosity μ_l and surface tension γ, falling through a gas of constant density ρ_g and viscosity μ_g, in a gravitational field with a constant acceleration due to gravity g. For convenience of analysis, all the variables and parameters are made dimensionless by measuring length in units of the volume-equivalent drop radius R, fluid flow velocity $\boldsymbol{v}$ in units of drop terminal velocity U and pressure p in units of $\mu_g U/R$. By measuring fluid density in units of ρ_g and viscosity in units of μ_g, the dimensionless liquid density and viscosity are denoted by ρ ($\equiv \rho_l/\rho_g$) and μ ($\equiv \mu_l/\mu_g$), while those for the surrounding gas become unity. A reference frame moving with the liquid drop is adopted here with the coordinate origin fixed at the centre of mass of the drop. Then, the axisymmetric laminar flow inside and outside the drop is governed by the steady incompressible Navier–Stokes equations

$$\frac{\rho}{2} Re\, \boldsymbol{v}\cdot\nabla\boldsymbol{v} = \nabla\cdot\boldsymbol{T}_l \quad \text{with} \quad \boldsymbol{T}_l \equiv -p\boldsymbol{I} + \mu[\nabla\boldsymbol{v} + (\nabla\boldsymbol{v})^T], \quad \nabla\cdot\boldsymbol{v} = 0, \tag{2.1}$$

and

$$\tfrac{1}{2} Re\, \boldsymbol{v}\cdot\nabla\boldsymbol{v} = \nabla\cdot\boldsymbol{T}_g \ \text{ with } \ \boldsymbol{T}_g \equiv -p\boldsymbol{I} + \nabla\boldsymbol{v} + (\nabla\boldsymbol{v})^T, \quad \nabla\cdot\boldsymbol{v} = 0, \tag{2.2}$$

where Re denotes the Reynolds number defined as $2\rho_g U R/\mu_g$, $\boldsymbol{I}$ the identity tensor and superscript 'T' stands for the transpose. Here p denotes the generalized pressure (which is also called piezometric pressure) that includes the term for hydrostatic pressure in the bulk of incompressible fluid, similar to the treatment of Dandy & Leal (1989). Thus, the gravitational (body) force term does not explicitly appear in (2.1) and (2.2); the hydrostatic pressure effect due to buoyancy force appears only in the traction boundary condition at free-fluid interface.

A cylindrical (z, r)-coordinate system is used here with the z-axis coinciding with the axis of symmetry and pointing in the direction opposite to that of the gravitational field. Thus, at the drop's free surface S_f conservation of momentum is satisfied by imposing the traction boundary condition

$$\boldsymbol{n}\cdot(\boldsymbol{T}_g - \boldsymbol{T}_l) = \frac{1}{Ca}\left(\frac{\mathrm{d}\boldsymbol{t}}{\mathrm{d}s} + \frac{\boldsymbol{n}}{r}\frac{\mathrm{d}z}{\mathrm{d}s}\right) - p_a\boldsymbol{n} + Stz\boldsymbol{n} \quad \text{on } S_f, \tag{2.3}$$

where $Ca \equiv \mu_g U/\gamma$ is the capillary number, the local unit normal vector $\boldsymbol{n}$ at the free surface points from the gas into liquid and the local unit tangent vector $\boldsymbol{t}$ points in the direction of increasing s (from the front stagnation point) along the free surface and relates to $\boldsymbol{n}$ in such a way that $\boldsymbol{n}\times\boldsymbol{t} = \boldsymbol{e}_\theta$ (with the right-handed cylindrical coordinate system (z, r, θ) being used in this study). The constant excess pressure inside the drop p_a is solved as an unknown to satisfy an overall constraint that the volume enclosed by the free surface S_f remains constant:

$$\int_{S_f} r^2 \frac{\mathrm{d}z}{\mathrm{d}s}\,\mathrm{d}s = \frac{4}{3}, \tag{2.4}$$

where the Stokes number $St \equiv (\rho - 1)\rho_g\, g\, R^2/(\mu_g U)$, representing the ratio of buoyancy force and viscous force, is also solved as an unknown to satisfy another overall constraint that the drop's centre of mass remains at the coordinate origin:

$$\int_{S_f} z\, r^2 \frac{\mathrm{d}z}{\mathrm{d}s}\,\mathrm{d}s = 0. \tag{2.5}$$

As already mentioned, the hydrostatic pressure effect due to buoyancy force now appears in the boundary condition (2.3) through St.

Moreover, the flow velocity field must satisfy

$$\boldsymbol{n}\cdot\boldsymbol{v}=0 \quad \text{on } S_f \text{ and } r=0, \tag{2.6}$$

at the free surface S_f, due to the kinematic condition, and at the axis of symmetry ($r=0$), as required by the symmetry condition. In addition, the stress-free symmetric condition at the axis of symmetry ($r=0$) can be expressed as

$$\boldsymbol{e}_z\boldsymbol{e}_r : \boldsymbol{T}=0 \quad \text{at} \quad r=0, \tag{2.7}$$

where $\boldsymbol{e}_z$ and $\boldsymbol{e}_r$ denote the unit vectors in the z- and r-directions, respectively. (Here $\boldsymbol{T}$ without the subscript 'l' or 'g' represents the hydrodynamic stress tensor in both phases.)

Among several treatments of the far-field boundaries, the simplest way for the present problem is to consider a cylindrical container wall with large enough radius (e.g. $10\times R$), with its centreline coinciding with the axis of symmetry of the falling liquid drop. Strictly speaking, the problem considered here is a liquid drop falling through a gas along the centreline of a cylindrical pipe of radius $10\times R$. However, the pipe-wall effect becomes inconsequential when Re is not small. As demonstrated in the grid study of Haywood *et al.* (1994*a*), the differences in drag coefficient between far-field boundary located at $10\times R$ and ∞ become less than 2 % for $Re>10$. Thus, at the cylindrical container wall ($r=10$) and the upstream (or 'inlet') boundary (e.g. located at $z=-10$ in figure 1), the Dirichlet type of condition for uniform flow velocity is specified as

$$\boldsymbol{v}=\boldsymbol{e}_z \quad \text{on} \quad r=10 \text{ and } S_{inlet}. \tag{2.8}$$

At the downstream (or 'outflow') boundary (e.g. located at $z=15$ in figure 1), a fully developed flow condition for hydrodynamic stresses is used, i.e.

$$\boldsymbol{e}_z\boldsymbol{e}_r : \boldsymbol{T}_g=\frac{\partial v_z}{\partial r} \quad \text{and} \quad \boldsymbol{e}_z\boldsymbol{e}_z : \boldsymbol{T}_g=0 \quad \text{on } S_{outlet}. \tag{2.9}$$

As exemplified by Feng & Scott (1996), Bozzi *et al.* (1997) and Feng (2007), among others, solutions to this type of free-boundary problem can be computed by discretizing the partial differential equation system (2.1)–(2.9) with the Galerkin method of weighted residuals using finite-element basis functions (cf. Strang & Fix 1973; Kistler & Scriven 1983). In doing so, the problem domain is divided into a set of quadrilateral elements (cf. figure 1), with biquadratic basis functions being used for expanding the velocity field and linear discontinuous basis functions for pressure. The distribution of finite-element mesh points around the deformable free surface is determined by a pair of elliptic partial differential equations that are also discretized by the Galerkin finite-element method using subparametric mapping (cf. de Santos 1991; Christodoulou & Scriven 1992). Then, the set of nonlinear algebraic equations of Galerkin's weighted residuals is simultaneously solved by Newton's method of iterations (Ortega & Rheinboldt 1970). At each Newton iteration, the Jacobian matrix of sensitivities of residuals to unknowns is evaluated with the values of unknowns determined in the previous iteration. The resulting linear algebra system is then solved by direct factorization of the Jacobian matrix with a modified version of Hood's (1976) frontal solver. The iteration is continued until the L_2 norm of the residual vector becomes less than 10^{-8}.

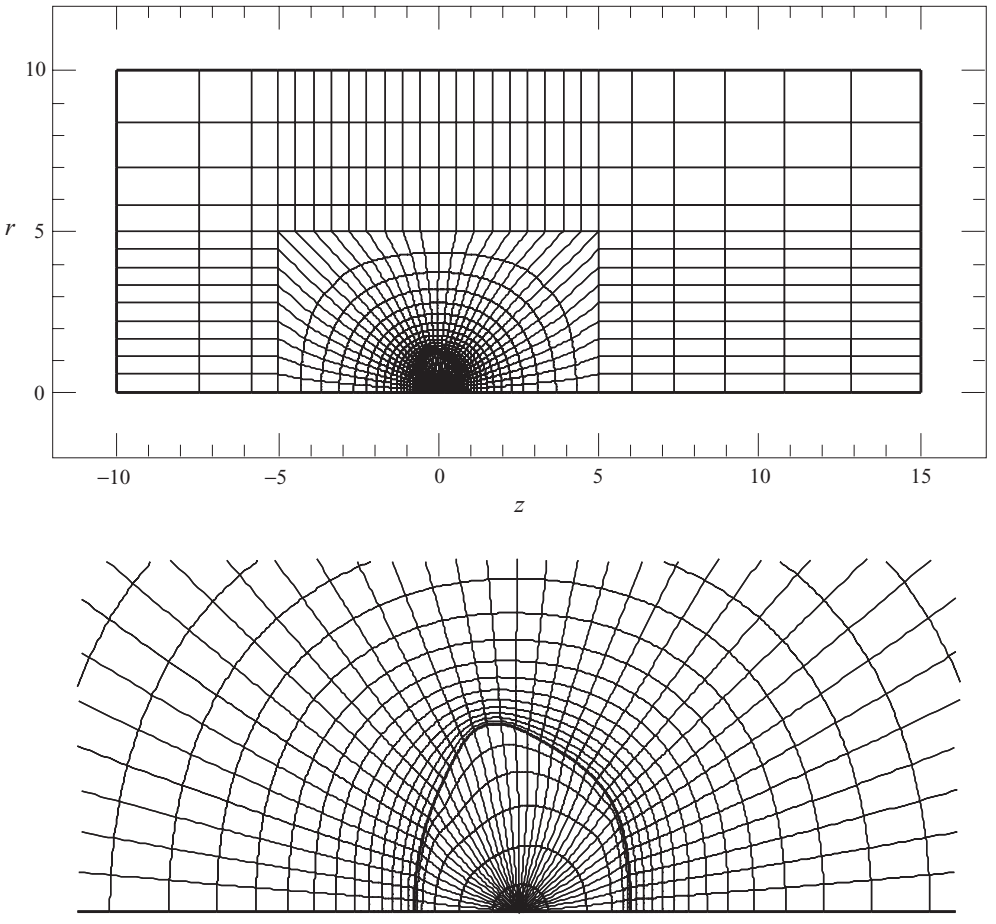

FIGURE 1. Finite-element mesh of the problem domain (as exemplified by the case of $\rho = 1000$, $\mu = 100$, $Re = 500$ and $We = 15$). The upper panel shows the entire problem domain and the lower panel the mesh distribution around the drop surface.

With the present mathematical formulation, the Reynolds number Re, capillary number Ca, (dimensionless) liquid density ρ and (dimensionless) liquid viscosity μ are the four independent parameters that can be conveniently specified, with St determined as part of the solution. Once Re, Ca, ρ, μ and St are given, all other relevant dimensionless parameters associated with a solution can be calculated. For example, the drag coefficient C_D, the Weber number We, the Ohnesorge number Oh, the Morton number Mo and the Eötvös number Eo (which is also called the Bond number) can be evaluated as follows:

$$\left.\begin{aligned} C_D &\equiv 8R\,g\,(\rho-1)/(3\,U^2) = 16St/(3Re), \\ We &\equiv 2\,\rho_g\,U^2\,R/\gamma = Re\,Ca, \\ Oh &\equiv \mu_l/\sqrt{2\,\rho_l\,\gamma\,R} = \mu\sqrt{We/\rho}\,/Re, \\ Mo &\equiv g\,\mu_g^4(\rho-1)/(\rho_g\,\gamma^3) = 3\,C_D\,We^3/(4\,Re^4), \\ Eo &\equiv 4\,(\rho-1)\rho_g\,g\,R^2/\gamma = 3\,C_D\,We/4 = Mo\,Re^4/We^2. \end{aligned}\right\} \tag{2.10}$$

Re	We	C_D	α	$2R$ (mm)	U (m s^{-1})	γ (N m^{-1})
100	1	1.1349	1.070	0.580	2.58	4.64×10^{-3}
	0.5	1.1156	1.034	0.577	2.60	9.35×10^{-3}
	0.1	1.0999	1.007	0.575	2.61	4.70×10^{-2}
200	1	0.7961	1.048	0.819	3.66	1.32×10^{-2}
	0.5	0.7853	1.024	0.815	3.68	2.65×10^{-2}
	0.1	0.7767	1.005	0.812	3.69	1.33×10^{-1}
300	1	0.6456	1.035	1.000	4.50	2.43×10^{-2}
	0.5	0.6391	1.018	0.997	4.51	4.87×10^{-2}
	0.1	0.6339	1.004	0.994	4.53	2.45×10^{-1}

TABLE 1. Values of given Re and We with computed C_D, α, $2R$ and U for a drop of $\rho = 1000$ and $\mu = 100$ in a gas (e.g. air) of $\rho_g = 1.2\,\mathrm{kg\ m^{-3}}$, $\mu_g = 1.8 \times 10^{-5}\,\mathrm{N\ s\ m^{-2}}$, with the gravitational acceleration $g = 9.8\,\mathrm{m\ s^{-2}}$.

By virtue of dynamical similarity (as discussed by Batchelor 1967), each solution to the non-dimensional governing equations for a set of specified Re, Ca, ρ and μ can represent numerous seemingly different fluid systems and drop sizes.

3. Computational results

In view of the fact that densities of common liquids (such as water, cooking oil, ethylene glycol, cresol, etc.) are around 1000 kg m^{-3}, while those of common gases (e.g. air, oxygen, nitrogen, etc. near the surface of the Earth) are around 1 kg m^{-3}, cases with ρ set at 1000 may be considered the most representative of a liquid drop in a gas. (In fact, it is rare to find a liquid with density less than 700 kg m^{-3}, such as that of gasoline, and more than 1500 kg m^{-3}, such as that of chloroform.) For viscosity, typical values for common gases are in the range between 1×10^{-5} and 3×10^{-5} N s m^{-2}, whereas that for water is 1×10^{-3} N s m^{-2} which is at the low end for liquids. Hence, the most representative value of μ for a liquid drop in a gas might be $\sim$100 (although $\mu = 50$ might be a closer approximation for a water drop in air).

Because successful solution of nonlinear equations by Newton iterations relies on sufficiently accurate initial estimates of the solution, it is often convenient to start by computing cases at small We and Re for nearly spherical drops. For example, with the present computational code (which is called the finite-element computational analysis widget (FECAW) accessible from http://sites.google.com/site/jamesqfeng/), a solution for $\rho = 1000$ and $\mu = 100$ at $We = 0.01$ and $Re = 1$ can be obtained easily from scratch (e.g. $\boldsymbol{v} = \boldsymbol{0}$ and $p = 0$) in a few Newton iterations. Once a solution for a given set of parameters is obtained, it can be used as an effective initial estimate for another nearby solution corresponding to one or more parameters being varied slightly in the parameter space. Thus, solutions for almost any set of parameters, if they exist, can be computed by varying the parameters in small steps from a 'first' solution. Such a simple scheme for tracking a family of solutions is sometimes called zeroth-order continuation.

Table 1 provides a list of results at small values of We for nearly spherical drops with $\rho = 1000$ and $\mu = 100$ for $Re = 100$, 200 and 300. With the solution for specified values of Re and Ca (or We), the drag coefficient C_D can be determined from the computed value of St according to (2.10). From the nodal coordinates along the drop

surface, the axis ratio

$$\alpha \equiv \frac{2r_{max}}{z_{max} - z_{min}} \tag{3.1}$$

can be calculated readily, where r_{max} is the radius of the drop cross-section (i.e. $2r_{max}$ represents the maximum transverse dimension), and z_{min}, z_{max} denote minimum and maximum z-coordinate values on the drop surface. If the values of ρ_g, μ_g and g are also specified, dimensional diameter $2R$ and terminal velocity U of the drop can then be determined from

$$\left.\begin{aligned} 2R &= \left\{4\mu_g^2\, Re\, St/[g\,\rho_g^2\,(\rho-1)]\right\}^{1/3} = \left\{3\mu_g^2\, Re^2\, C_D/[4\,g\,\rho_g^2\,(\rho-1)]\right\}^{1/3}, \\ U &= [g\,\mu_g\,(\rho-1)\,Re^2/(4\,\rho_g\,St)]^{1/3} = [4\,g\,\mu_g\,(\rho-1)\,Re/(3\,\rho_g\,C_D)]^{1/3}. \end{aligned}\right\} \tag{3.2}$$

With the known value of U determined from (3.2), the corresponding value of surface tension γ can be obtained from

$$\gamma = \frac{\mu_g\, U}{Ca}. \tag{3.3}$$

Considering the fact that water has a surface tension $\sim$0.07 N m^{-1} and many liquids have surface tension less than that of water but usually $>$0.01 N m^{-1}, a liquid drop of $2R \sim 1$ mm falling through a gas under normal conditions near the surface of the Earth is expected to have $Re \sim 300$ and We between 0.3 and 1. This suggests that a liquid drop falling through a gas with $Re < 100$ can rarely have We exceeding unity, with noticeable drop deformations (cf. table 1). Therefore, cases with $Re <$100 are not to be emphasized here for their deformations are not expected to be representative of liquid drops falling through gases (whereas cases for smaller ρ and μ relevant to a deformable liquid drop moving through another liquid or in a high-temperature, high-pressure gas have been mostly covered by Dandy & Leal (1989) and Helenbrook & Edwards (2002), among others).

At $Re = 100$ and $We = 0.1$ with $\rho = \mu = 1000$, the drop is expected to behave just like a rigid sphere because the axis ratio $\alpha = 1.0089$ and the maximum internal circulation velocity $v_{ic} = 2.467 \times 10^{-3}$. The drag coefficient computed here for this case is $C_D = 1.1081$, which is in very good agreement with 1.10 computed for a rigid sphere by LeClair *et al.* (1972) and 1.091 by Helenbrook & Edwards (2002) with their finest mesh. For $20 \leqslant Re \leqslant 260$, a correlation formula of C_D for rigid spheres moving in a fluid was recommended by Clift, Grace & Weber (1978) based on numerous experimental data as

$$C_D = \frac{24}{Re}(1 + 0.1935\, Re^{0.6305}), \tag{3.4}$$

which predicts $C_D = 1.087$, 0.7756 and 0.6444 for $Re = 100$, 200 and 300. The values of C_D computed here at $We = 0.1$ and $\rho = \mu = 1000$ for $Re = 200$ and 300 are 0.7848 and 0.6424, respectively, all within $\pm$2 % of that predicted by (3.4). Interestingly, extending (3.4) to $Re = 400$ and 500 yields $C_D = 0.5675$ and 0.5153, still agreeing quite well with 0.5559 and 0.4917, as computed here at $We = 0.1$ for $\rho = \mu = 1000$ (within 5 %). Thus, (3.4) can be useful for calculating the drag coefficient for steady axisymmetric motion of a rigid sphere (or a fluid drop with large values of ρ and μ but small We) in a fluid at least up to $Re = 500$, although a strictly steady axisymmetric drop at $Re > 200$ may not be realizable in a laboratory because of the onset of wake instability and vortex shedding (Clift *et al.* 1978).

Also as a comparison, the computed C_D becomes 1.0999 with $v_{ic} = 2.404 \times 10^{-2}$ and $\alpha = 1.0068$ if μ is reduced to 100 at $Re = 100$ and $We = 0.1$ with $\rho = 1000$. Actually,

the comparison between (3.4) and all the values of C_D shown in table 1 seems to be quite reasonable. Thus, a liquid drop falling through a gas under normal condition near the surface of the Earth at $Re \leqslant 300$ behaves practically the same as a rigid sphere. This is because of the typically large values of μ for liquid drops in gases that prevent the internal circulation inside the drop to become too intensive to significantly influence the drag force. This is also consistent with the general comment of Clift *et al.* (1978) that the drag coefficient for a liquid drop (usually of diameter less than 1 mm) differs little from that for a rigid sphere falling in a gas unless the drop-shape deformation becomes considerable (e.g. for drops with extremely low surface tension). However, the fluid mechanics problem of a liquid drop falling through a quiescent gas under the action of gravity can also be considered as a canonical problem for industrial and agricultural sprays, where the drop size is much smaller than the gas flow scales and the drop deformation, and internal circulation responses are faster than its velocity decay rate (which is usually satisfied when μ is large, according to the estimates of Helenbrook & Edwards 2002). In typical spray applications, the relative velocity of a drop with respect to the gas can be momentarily much larger than its terminal velocity in a gravitational field, and surface tension may be substantially reduced when temperature is high as in the situation of injected fuel droplets in a combustion chamber. Even a 100 μm fuel droplet may move at $Re \sim 100$ in a combustion chamber with $We \sim 2$ (Haywood *et al.* 1994*b*). Therefore, computing cases with We much larger than that considered in table 1 can also provide valuable knowledge relevant to understanding drop behaviour in spray and other applications.

Most results presented in this study are computed using the mesh shown in figure 1, with 1053 quadrilateral elements corresponding to 4359 nodes. A coarser mesh with 594 elements (corresponding to 2489 nodes) is sometimes used for checking the sensitivity of the results to mesh refinement. At $Re = 0$ and $Ca = 0.01$, the computed St is 5.6678 (or 5.6688 with the coarser mesh), which is in good agreement with 5.6612, as predicted by Haberman & Sayre (1958) for a spherical drop moving in a cylindrical tube of radius 10 times the drop radius for $\mu = 100$. Hence, a basic validation of the present domain size and meshing is obtained for the desired accuracy of the computed results. Among limited results published in the literature for deformable drops moving in gases at non-zero Re, Dandy & Leal (1989) presented a few computed values of C_D, e.g. $C_D = 1.61$ at $Re = 60$ and $We = 4$ for $\rho = 1000$ and $\mu = 100$, and $C_D = 1.29$ at $Re = 100$ and $We = 4$ for $\rho = 1000$ and $\mu = 200$. These data provide an important reference. As a comparison, the corresponding values of C_D computed here are 1.6700 (or 1.6709 with the coarser mesh) at $Re = 60$ and $We = 4$ for $\rho = 1000$ and $\mu = 100$, and 1.3269 (or 1.3278 with the coarser mesh) at $Re = 100$ and $We = 4$ for $\rho = 1000$ and $\mu = 200$. As was also shown by Helenbrook & Edwards (2002), the values of C_D computed here are slightly (by a few per cent) higher than that reported by Dandy & Leal (1989).

In the following, computed solutions for $\rho = 1000$ and $\mu = 100, \geqslant 200$ and 50 are presented in §§ 3.1, 3.2 and 3.3, respectively. Then, cases with variations of ρ and μ by $\pm 25\,\%$ (or more) from the nominal cases of $\rho = 1000$ with ρ/μ or ρ/μ^2 fixed are examined in § 3.4, to explore the possibility for extending the results for $\rho = 1000$ to cases with other values of ρ.

3.1. *Solutions for* $\rho = 1000$ *and* $\mu = 100$

Because the onset of wake eddy shedding is often observed at $Re \sim 200$ for drops with large μ (cf. Clift *et al.* 1978), cases where $Re = 200$ might be considered as the upper limit of Re for strictly steady axisymmetric drop motion under normal

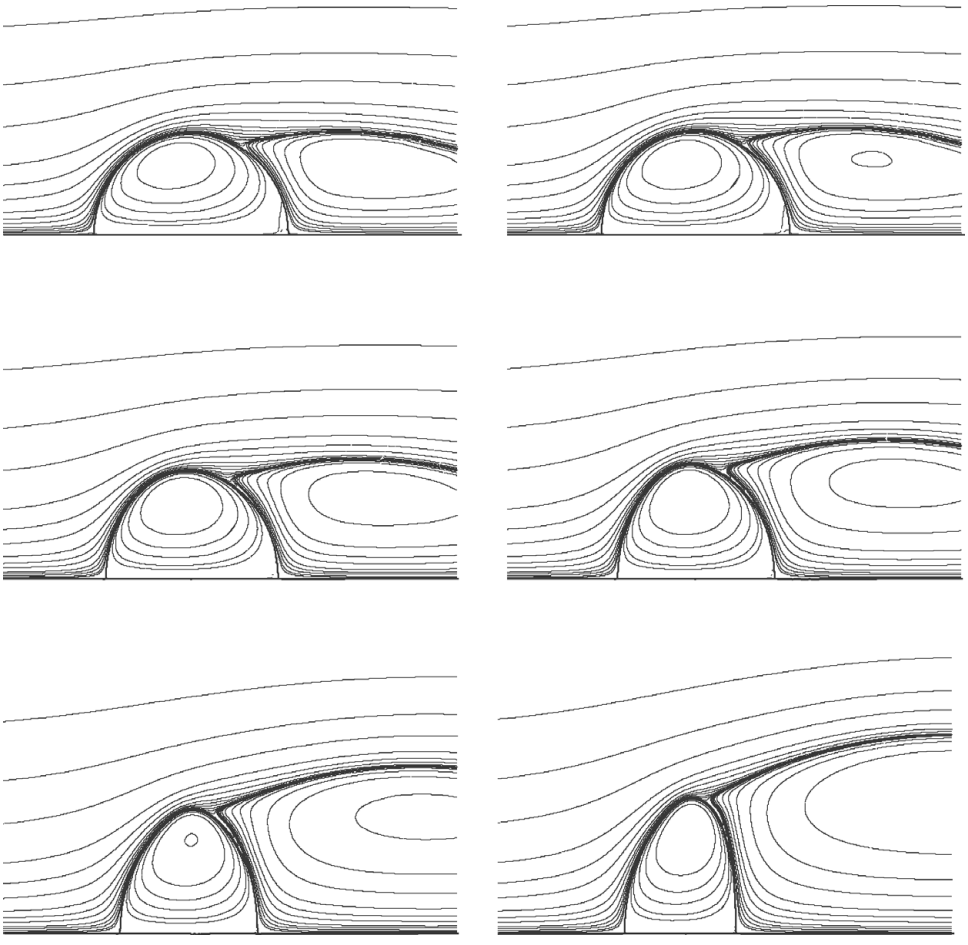

FIGURE 2. Streamlines and drop shapes (from $z = -2$ to $z = 3$) for $We = 1$, 2, 5, 8, 12 and 15 (left to right from top left to bottom right) at $Re = 200$ (with $\rho = 1000$ and $\mu = 100$). The contour values for streamfunctions shown here are 0, ± 0.0001, ± 0.0002, ± 0.0005, ± 0.001, ± 0.002, ± 0.005, ± 0.01, ± 0.02, ± 0.05, ± 0.1, etc.

conditions, although the steady axisymmetric solutions for $Re > 200$ may still be used to describe many observed falling drop behaviours. Figure 2 shows the streamlines and drop shapes for $We = 1$, 2, 5, 8, 12 and 15 at $Re = 200$, while table 2 provides the corresponding values of various computed parameters such as the drag coefficient C_D, the Eötvös number Eo, the maximum internal circulation velocity v_{ic} (on the drop surface), the polar angle (measured from the front stagnation point) θ_{ic} where the v_{ic} is located, the maximum r-coordinate on the drop surface r_{max}, the minimum z-coordinate on the drop surface z_{min}, the maximum z-coordinate on the drop surface z_{max}, the axis ratio α (according to (3.1)), the half-width of the wake r_{wake} and the z-coordinate at the axis of symmetry where the wake ends z_{wake} (as indicated by $v_z = 0$).

For large values of ρ (e.g. $\rho = 1000$) and μ (e.g. $\mu = 100$) at $Re \geqslant 100$, drop deformations are almost visually unnoticeable until $We \sim 5$. Significant (oblate) drop deformations appear at $We \geqslant 10$. Specifically at $Re = 200$ for $\rho = 1000$ and $\mu = 100$, the drop deforms in an almost fore–aft symmetric manner with increasing We up

We	C_D	Eo	v_{ic}	θ_{ic} (deg.)	r_{max}	z_{min}	z_{max}	α	r_{wake}	z_{wake}
1	0.7955	0.5966	3.207×10^{-2}	67.8	1.016	−0.966	0.972	1.049	1.024	3.942
2	0.8175	1.2262	3.328×10^{-2}	68.2	1.032	−0.934	0.945	1.099	1.071	4.069
5	0.8918	3.3441	3.688×10^{-2}	73.7	1.081	−0.845	0.869	1.261	1.190	4.486
8	0.9961	5.9764	3.929×10^{-2}	78.7	1.145	−0.771	0.790	1.466	1.382	5.054
12	1.1427	10.285	3.775×10^{-2}	84.2	1.241	−0.707	0.663	1.812	1.671	5.810
15	1.3274	14.933	3.547×10^{-2}	86.7	1.353	−0.609	0.500	2.440	1.980	6.571

TABLE 2. Values of We, C_D, Eo, v_{ic}, θ_{ic}, r_{max}, z_{min}, z_{max}, α, r_{wake} and z_{wake} for $Re = 200$ ($\rho = 1000$ and $\mu = 100$).

to $We = 15$. As shown by Dandy & Leal (1989), the streamlines indicate that the recirculating wakes are detached from the drop surface for the most part because of the absence of a substantial secondary interior recirculating vortex inside the drop. The relative intensity of internal circulation (denoted as v_{ic} and measured in units of terminal velocity U) increases with We up to ~8 and then decreases with further increasing We. The reduction of v_{ic} at larger We could be a consequence of the narrowing space within the severely deformed drop. Not surprisingly, the size (or volume) of the recirculating wake increases with We, which is consistent with both mechanisms for vorticity generation: from a curved free surface and from a bluff body of considerable transverse dimension (cf. Batchelor 1967) which increases with enhanced oblate drop deformation.

As a reference, the value of Ohnesorge number Oh at $We = 15$ and $Re = 200$ for $\rho = 1000$ and $\mu = 100$ is 0.0612. According to the arguments of Helenbrook & Edward (2002), based on comparing the velocity decay rate of the drop with its deformation response rate (as indicated by the results of Miller & Scriven 1968), drops are expected to respond, in a quasi-steady manner, to their instantaneous relative velocities with respect to the gas when $Oh \ll 1$ and $\mu \gg 1$. Therefore, the steady solutions computed here can also be used to describe the quasi-steady behaviour of drops injected into a gas, as in spray coating, even though the relative velocity of drops with respect to the gas changes with time.

When discussing experimental results for deformed liquid drops falling in air, Clift *et al.* (1978) presented a formula by fitting the measurement data for the axis ratio α as

$$\alpha = \begin{cases} 1.0 & \text{when } Eo \leqslant 0.4, \\ 1.0 + 0.18\,(Eo - 0.4)^{0.8} & \text{when } 0.4 < Eo < 8. \end{cases} \tag{3.5}$$

With the values of Eo given in table 2 for $We = 1$, 2, 5, 8, 12 and 15, (3.5) yields $\alpha = 1.049$, 1.155, 1.427, 1.712, 2.125 and 2.530, which seems to consistently over-estimate the drop deformation when compared with that computed according to (3.1) in table 2 (for $\rho = 1000$ and $\mu = 100$). Interestingly, the agreement between (3.5) and computed α seems to improve somewhat for $We = 15$ despite the fact that the corresponding Eo is far beyond 8.

Among several correlation formulas for the drag coefficient of deformable drops, the most straightforward one seems to come from the intuition that the drag force may simply be described using the radius of cross-sectional area r_{max} to modify Re in (3.4) such that the drag coefficient for a deformable drop becomes

$$C_D = \frac{24\, r_{max}}{Re}\left[1 + 0.1935\,(r_{max}\, Re)^{0.6305}\right], \tag{3.6}$$

which is similar to a formula proposed by Helenbrook & Edwards (2002) using $\alpha^{1/3}$ instead of r_{max}. Here the effect of internal circulation is ignored because it is generally weak in a liquid drop falling in a gas with large μ. Substituting the values of r_{max} given in table 2 into (3.6) with $Re = 200$ yields $C_D = 0.7947$, 0.8140, 0.8741, 0.9550, 1.0812 and 1.2343, respectively, for $We = 1$, 2, 5, 8, 12 and 15, which are quite comparable to the values of C_D presented in table 2.

As is known for drops and bubbles, continuation by increasing We (or reducing the surface-tension effect) at a given Re would usually reach a turning point (or singular point as the Jacobian matrix for the Newton iterations becomes singular with rank deficiency of 1), beyond which steady axisymmetric solutions do not (locally) exist for a deformable drop or bubble (cf. Feng 2007). This phenomenon is sometimes called 'shape instability'. Physically, the turning point indicates the incipience of instability (Iooss & Joseph 1990), suggesting that the deforming stresses at the drop surface, arising from the flow field, become so strong that surface tension can no longer hold the drop together. For the case of $Re = 200$ with $\rho = 1000$ and $\mu = 100$, the critical Weber number We_c for the onset of shape instability is found to be 15.602, with $\alpha = 3.341$. Using an arclength-continuation algorithm (as in Feng 2000, 2007), solutions along the branch around turning points can still be computed, even though those after the branch folds back to reduced values of We are expected to be unstable even with respect to axisymmetric disturbances. Thus, at a given value of We (below We_c) there can be two different solutions: one corresponds to the stable drop and the other to the unstable drop. The unstable drop usually corresponds to the one with more severe deformation, or in other words, larger axis ratio α. For example, as the solution folds from $We_c = 15.602$ back to $We = 15.5$ (for $Re = 200$ at $\rho = 1000$ and $\mu = 100$) the unstable drop has an axis ratio $\alpha = 4.071$, having disc-like shape with a thinning centre, indicating the development of dimples at both the front and rear stagnation points – a precursor of a typical break-up mode (Clift *et al.* 1978).

Noteworthy here is that a deformable drop in a flow field is susceptible to several different types of instabilities. As commented by Ryskin & Leal (1984), the shape instability discussed here should be distinguished from the path instability associated with non-rectilinear trajectories intrinsically due to unsteady wake flows (for which a recent summary was provided by Yang & Prosperetti 2007). In principle, the path instability can occur at relatively low We with very slight free-surface deformation, whereas shape instability does not have to be induced by an unsteady wake. For example, a drop in a static electric field without the presence of fluid flow can also exhibit shape instability when the electric field strength exceeds a critical value (cf. Taylor 1964).

Figure 3 shows the streamlines and drop shapes for $We = 10$ at $Re = 50$, 100, 200, 300, 400 and 500, while table 3 provides the corresponding values of various computed parameters (as in table 2). For cases of $Re < 200$, the deformed drops tend to develop a flattened or even dimpled rear surface while the front surface remains rounded. Detachment of the recirculating wake becomes obvious with the drop at $Re = 50$ having a free-surface profile of the 'kidney-bean' shape with $Mo = 2.68 \times 10^{-4}$. At $Re = 200$, the drop deformation is nearly fore–aft symmetric. Then for $Re > 200$ the front surface becomes increasingly flattened with increasing Re, while the rear surface stays somewhat rounded. Remarkable here (from table 3) is that the drop's axis ratio α decreases with increasing Re. Yet the volume of the recirculating wake generally increases with Re (for fixed We), consistent with increased free-surface curvatures at higher Re indicated by sharper free-surface

Re	C_D	Eo	v_{ic}	θ_{ic} (deg.)	r_{max}	z_{min}	z_{max}	α	r_{wake}	z_{wake}
50	2.2320	16.740	2.636×10^{-2}	87.1	1.264	−0.694	0.500	2.117	1.190	3.107
100	1.5820	11.865	3.310×10^{-2}	86.6	1.248	−0.703	0.576	1.952	1.375	4.435
200	1.0735	8.0511	3.884×10^{-2}	81.3	1.193	−0.736	0.730	1.628	1.538	5.463
300	0.8524	6.3930	4.074×10^{-2}	78.4	1.157	−0.747	0.795	1.501	1.656	5.889
400	0.7180	5.3847	4.077×10^{-2}	72.7	1.127	−0.753	0.829	1.425	1.775	5.939
500	0.6228	4.6712	3.994×10^{-2}	71.3	1.101	−0.762	0.854	1.363	1.838	5.825

TABLE 3. Values of Re, C_D, Eo, v_{ic}, θ_{ic}, r_{max}, z_{min}, z_{max}, α, r_{wake} and z_{wake} for $We = 10$ ($\rho = 1000$ and $\mu = 100$).

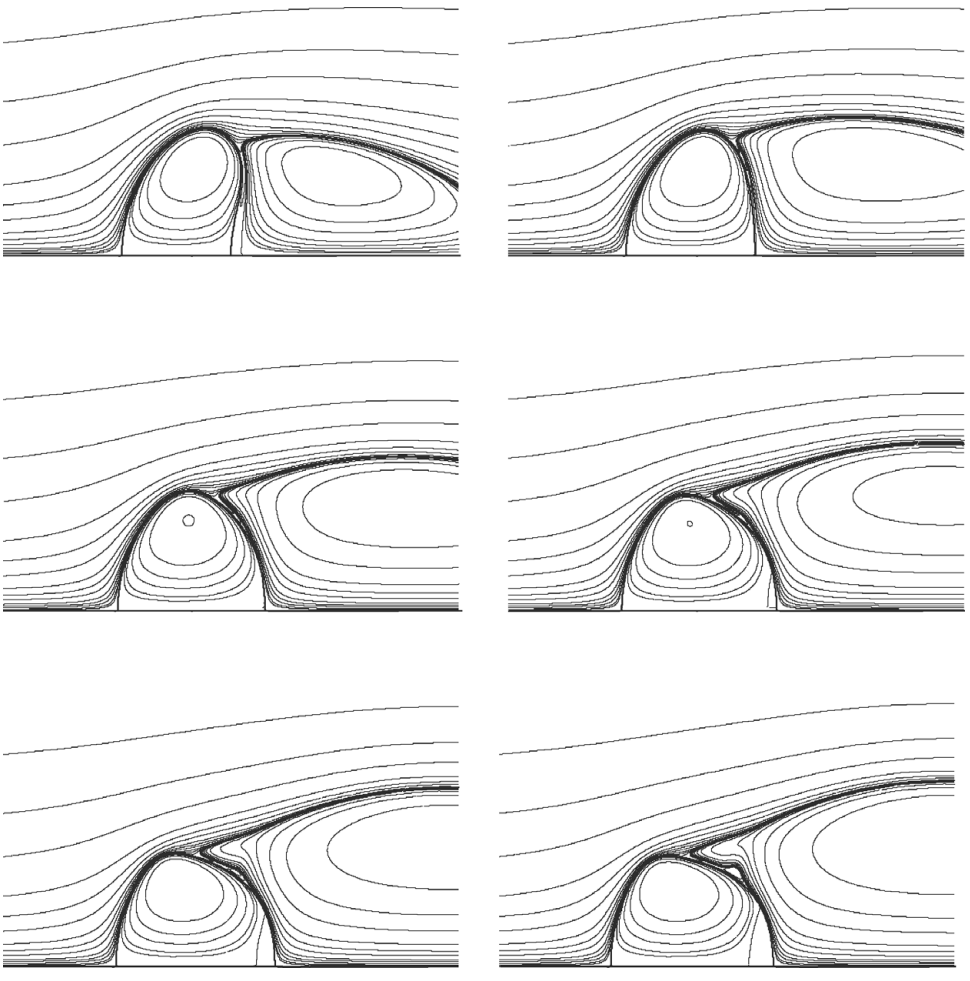

FIGURE 3. Same as figure 2, but for $We = 10$ at $Re = 50$, 100, 200, 300, 400 and 500.

bendings on drops at $Re = 400$, 500 (see figure 3) despite the reduced values of α. Accompanying these sharp free-surface bendings is the complicated local flow field in the detached recirculating wake adjacent to the rear surface of the drop. However, the wake length z_{wake} (but not wake width) seems to decrease slightly from $Re = 400$ to 500, apparently consistent with the mechanism for vorticity

generation from a bluff body of reduced transverse dimension $2r_{max}$. Because of the shape deformation, the relation of the length of wake behind a deformable drop and Re seems to exhibit more complicated behaviour than that of a rigid sphere with both wake length and width always increasing with Re (cf. Fornberg 1988) due to the slower viscous diffusion of vorticity and stronger convection effect at higher Re. Similar to that observed by Dandy & Leal (1989), with increasing Re the internal circulation vortex is gradually shifted towards the front of the drop, as indicated by θ_{ic} in table 3.

For cases in table 3 for $Re = 50$, 100, 200, 300, 400 and 500, (3.5) yields $\alpha = 2.683$, 2.268, 1.917, 1.754, 1.651 and 1.575, which again seem to over-estimate the axis ratio compared to that given in table 3. If (3.6) is used with Re and r_{max} given in table 3, $C_D = 2.2100$, 1.5151, 1.0174, 0.8085, 0.6834 and 0.5987 are obtained, for $Re = 50$, 100, 200, 300, 400 and 500 at $We = 10$, respectively, slightly under-estimating C_D by $\sim$5 %.

As expected, the critical Weber number We_c for 'shape instability', as illustrated for the case of $Re = 200$, can also be determined by arclength continuation for other values of Re. Thus, we have $We_c = 13.521$ with $\alpha = 3.312$ for $Re = 100$, $We_c = 15.602$ with $\alpha = 3.341$ for $Re = 200$, $We_c = 17.491$ with $\alpha = 2.809$ for $Re = 300$ and $We_c = 19.591$ with $\alpha = 2.778$ for $Re = 500$. A trend seems to emerge for increasing We_c with Re (for $\rho = 1000$ and $\mu = 100$).

3.2. *Solutions for* $\rho = 1000$ *and* $\mu \geqslant 200$

Intuitively, increasing the viscosity ratio μ should reduce the internal circulation intensity, which is already quite weak at $\mu = 100$. One might wonder at what value of μ the internal circulation effect becomes negligible and thereafter further increasing μ presents no further noticeable changes in the drop behaviour. Figure 4 shows comparative streamlines and drop shapes with $\mu = 200$ and 1000 for $Re = 100$, 300 and 500 at $We = 10$, while table 4 provides the corresponding values of various computed parameters as in table 2, with additional data provided for $\mu = 400$. Interestingly, the drop shapes and external flow fields (at given values of Re and We) for $\mu = 200$ are basically the same as those for $\mu = 1000$ (and also for $\mu = 400$), except the further reduced internal circulation intensity v_{ic}, which is expected to be weak enough to have an inconsequential effect on the drop deformation and external gas flow field.

However, a slightly enhanced 'oblate' deformation and increased recirculating wake size with increasing μ can still be observed especially at $Re = 300$ and 500 (see table 4, although visually difficult to detect in figure 4). At these larger Re, the internal circulation vortex is also shifted slightly towards the front of drop with increasing μ. The length of the wake does not always increase with Re, as illustrated in table 4 with z_{wake} at $Re = 300$ being greater than that at $Re = 500$. But the width of the wake appears to consistently increase with Re if all other parameters are fixed. Compared with figure 3, drops in figure 4 at increased μ exhibit smoother surface profiles, suggesting that the complexity in drop surface profiles at $\mu = 100$ could be a consequence of the internal circulation effect.

Comparison of the drop shapes at corresponding values of Re between figures 3 and 4 (both at $We = 10$) demonstrates a trend of increasing drop axis ratio α with more flattened front surface and decreasing internal recirculation intensity v_{ic} as μ increases. This is consistent with the common understanding that the dynamic pressure forces external to the drop tend to push the regions near stagnation points inwards (Dandy & Leal 1989; Helenbrook & Edwards 2002). However, the dynamic pressure forces from inside the drop due to internal circulation tend to do the opposite, namely to

Re	μ	C_D	Eo	v_{ic}	θ_{ic} (deg.)	r_{max}	z_{min}	z_{max}	α	r_{wake}	z_{wake}
100	200	1.7941	13.456	1.873×10^{-2}	82.6	1.327	−0.582	0.459	2.549	1.553	5.040
	400	1.8457	13.842	9.673×10^{-3}	81.8	1.344	−0.549	0.445	2.704	1.601	5.183
	1000	1.8590	13.943	3.910×10^{-3}	81.8	1.348	−0.541	0.443	2.740	1.613	5.220
300	200	0.9540	7.1544	2.568×10^{-2}	75.8	1.229	−0.625	0.664	1.907	1.925	6.318
	400	0.9844	7.3819	1.351×10^{-2}	74.1	1.248	−0.584	0.626	2.063	2.002	6.457
	1000	0.9936	7.4520	5.468×10^{-3}	73.2	1.253	−0.571	0.614	2.115	2.012	6.492
500	200	0.6751	5.0634	2.722×10^{-2}	71.8	1.169	−0.666	0.739	1.664	2.075	5.897
	400	0.6979	5.2345	1.501×10^{-2}	70.1	1.190	−0.630	0.704	1.784	2.145	5.939
	1000	0.7058	5.2936	6.078×10^{-3}	68.8	1.196	−0.616	0.692	1.829	2.173	5.950

TABLE 4. Values of Re, μ, C_D, Eo, v_{ic}, θ_{ic}, r_{max}, z_{min}, z_{max}, α, r_{wake} and z_{wake} for $We = 10$ ($\rho = 1000$).

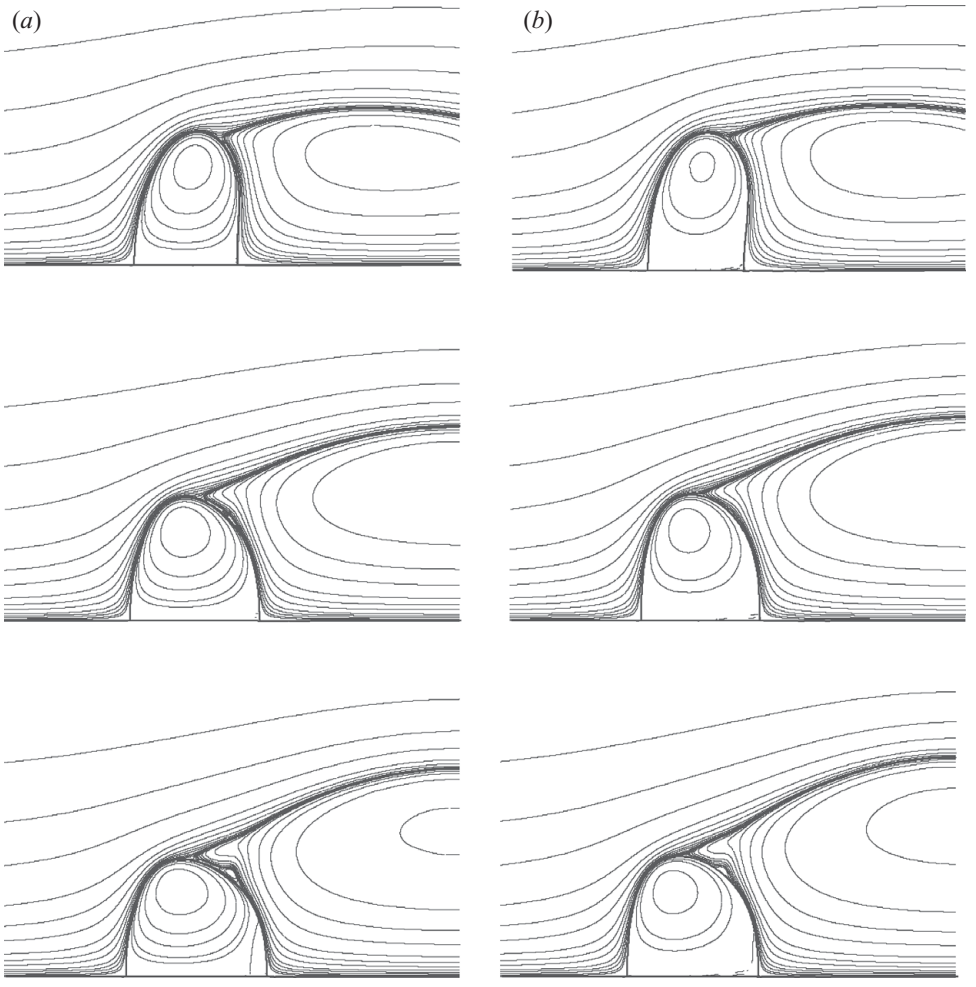

FIGURE 4. Same as figure 2, but for $We = 10$ at $Re = 100$ (top row), 300 (middle row) and 500 (bottom row), each having $\mu = 200$ in (a) and 1000 in (b) (with $\rho = 1000$).

We	C_D	Eo	v_{ic}	θ_{ic} (deg.)	r_{max}	z_{min}	z_{max}	α	r_{wake}	z_{wake}
5	1.1120	4.1701	4.565×10^{-2}	71.5	1.015	−0.964	0.951	1.060	0.834	2.759
10	1.1289	8.4666	4.734×10^{-2}	72.9	1.022	−0.940	0.918	1.100	0.853	2.815
100	1.1631	87.234	4.875×10^{-2}	76.9	1.047	−0.912	0.789	1.231	0.900	2.943

TABLE 5. Values of We, C_D, Eo, v_{ic}, θ_{ic}, r_{max}, z_{min}, z_{max}, α, r_{wake} and z_{wake} for $Re = 100$ ($\rho = 1000$ and $\mu = 50$).

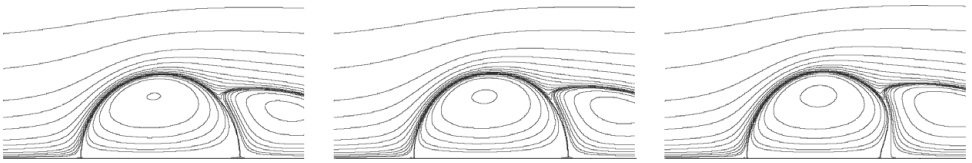

FIGURE 5. Streamlines and drop shapes (from $z = -2$ to $z = 2$) for $We = 5$ (left), 10 (middle) and 100 (right) at $Re = 100$ (with $\rho = 1000$ and $\mu = 50$).

push regions near stagnation points outwards (Helenbrook & Edwards 2002). For $\mu = 200$ at $Re = 300$, the critical Weber number We_c for the onset of 'shape instability' becomes 16.297, lowered from that for $\mu = 100$, with $\alpha = 4.294$ for a disc-shaped drop with a thinning centre from the shallow dimple on the front surface. This is expected because of more enhanced drop deformations being observed at larger μ.

For cases in table 4 at $Re = 100$, 300 and 500 with $\mu = 200$, (3.5) yields $\alpha = 2.406$, 1.830 and 1.617, whereas those given in table 4 are 2.549, 1.907 and 1.664. In contrast to the drops of $\mu = 100$, (3.5) now seems to slightly under-estimate the axis ratio. Increasing μ beyond 200 tends only to deteriorate such an under-estimation of (3.5). This suggests that the experimental measurements of axis ratios used for fitting (3.5) must have been with drops of either $\mu \sim 200$ or in the presence of surface contaminants that reduce the internal circulation intensity v_{ic} to the level around 0.02–0.03 (with $\rho \sim 1000$). (It is usually difficult to eliminate surface-active contaminants in systems of practical importance; most of the experimental results in the literature are for 'grossly contaminated' drops, according to Clift *et al.* 1978.) When $v_{ic} > 0.03$, as for cases with $\mu \sim 100$, (3.5) tends to over-estimate the axis ratio; on the other hand, it under-estimates α when $v_{ic} < 0.02$, as for cases with $\mu > 200$.

Substituting the values of r_{max} and Re for the corresponding cases in table 4 into (3.6) yields $C_D = 1.6620$, 1.6942, 1.7018, 0.8883, 0.9098, 0.9155, 0.6589, 0.6777 and 0.6831, within 10 % of the computed C_D in table 4 even for $r_{max} > 1.3$. Therefore, (3.6) can become a practically useful approximating formula for a liquid drop moving in a gas, considering its simplicity and reasonable accuracy.

3.3. *Solutions for* $\rho = 1000$ *and* $\mu = 50$

To examine the intensified internal circulation effect, cases with $\mu = 50$ (which are relevant to low-viscosity liquid drops in gases such as water drops in air) are computed here. Figure 5 shows the streamlines and drop shapes for $We = 5$, 10 and 100 at $Re = 100$ and $\mu = 50$, while table 5 provides the corresponding values of various computed parameters as in table 2. In contrast to cases with $\mu \geqslant 100$, drops of $\mu = 50$ at $Re = 100$ appear reluctant to deform into an oblate shape; even at $We = 100$ the

We	C_D	Eo	v_{ic}	θ_{ic} (deg.)	r_{max}	z_{min}	z_{max}	α	r_{wake}	z_{wake}
5	0.7163	2.6862	4.988×10^{-2}	69.2	0.948	−1.030	1.054	0.9098	0.853	3.388
10	0.7778	5.8337	5.447×10^{-2}	74.7	1.003	−0.944	0.996	1.034	0.957	3.706
100	0.8614	64.605	5.824×10^{-2}	76.6	1.067	−0.846	0.801	1.296	1.100	4.256

TABLE 6. As in table 5 but for $Re = 200$.

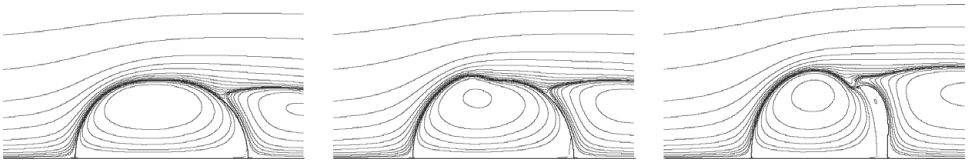

FIGURE 6. Same as figure 5 but at $Re = 200$.

drop deformation is still rather moderate compared to that of $\mu \geqslant 100$ at $We = 10$. If We is increased further, the dimple shown at the rear of the drop (for $We = 100$) would grow deeper into the drop. Eventually at $We = 333$, a cusp-like profile is formed at the rear central stagnation point. This kind of drop shape appears very similar to that of a dimpled shape shown by Helenbrook & Edwards (2002) for $\rho = 50$ and $\mu = 15$ at $Re = 5$ and $We = 5.5$. Yet the computed C_D (= 1.1558) and α (= 1.208) for the drop at $We = 333$ are not much different from those at $We = 100$ (i.e. 1.1631 and 1.231).

Because (3.5) is known to be reasonable only for cases with $\rho = 1000$ and $\mu \sim 200$, it is not surprising to see its inaccurate predictions for cases with $\rho = 1000$ and $\mu = 50$. For example, (3.5) would yield $\alpha = 1.52$ for $Eo = 4.17$ at $Re = 100$ and $We = 5$ whereas the value based on (3.1) is 1.06. In contrast, (3.6) has no difficulty in providing accurate estimates of C_D for the cases in table 5 as 1.1114, 1.1229 and 1.1642.

If Re is increased to 200, a drop of $\mu = 50$ deforms into a prolate shape (with $\alpha = 0.910$) at $We = 5$, and then its axis ratio α comes back to 1.034 at $We = 10$ with a shape quite different from that of a near spherical one (see figure 6) having a protruding rim in the front half of the drop. At $We = 100$, the drop in figure 6 shows a profile similar to the button mushroom (actually an 'upside-down' one if considering that the drop is falling from right to left in the plots). Prolate deformations of liquid drops falling in gases (with $\rho \leqslant 500$ and $\mu \leqslant 15$) were computed by Helenbrook & Edwards (2002), who suggested the tendency of internal circulation inside the drop to cause prolate drop deformations. For this reason, the prolate drop deformation is expected at smaller μ as is observed here at $\mu = 50$. However, the trend of disappearing prolate deformation with increasing We (for a drop of $\mu = 50$) is somewhat puzzling. In general, prolate drops are expected to be axisymmetrically unstable in view of the fact that falling solid ellipsoids tend to align with the long axis normal to the flow (Clift *et al.* 1978). Helenbrook & Edwards (2002) suspected that prolate drops would rather tumble in a three-dimensional fashion wobbling or oscillating while falling through a gas, to explain why prolate falling drops have never been reported in experimental observations.

Again, substituting the values of r_{max} at $Re = 200$ in table 6 into (3.6) yields values of C_D as 0.7147, 0.7792 and 0.8556, respectively, for $We = 5$, 10 and 100, which are

We	C_D	Eo	v_{ic}	θ_{ic} (deg.)	r_{max}	z_{min}	z_{max}	α	r_{wake}	z_{wake}
5	0.5538	2.0766	5.101×10^{-2}	63.4	0.907	−1.073	1.116	0.8287	0.843	3.690
10	0.6881	5.1607	5.424×10^{-2}	69.3	1.032	−0.906	0.975	1.097	1.176	4.737
100	0.7633	57.246	6.003×10^{-2}	77.8	1.104	−0.763	0.775	1.434	1.404	5.308

TABLE 7. As in table 5 but for $Re = 300$.

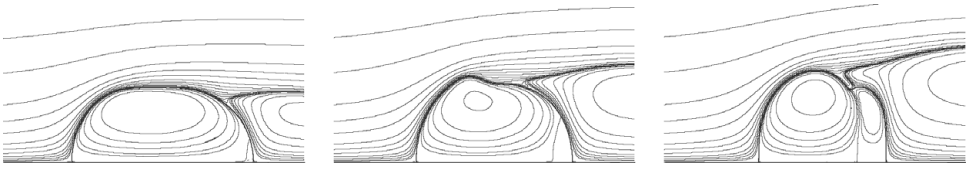

FIGURE 7. Same as figure 5 but at $Re = 300$.

in good agreement with those in table 6 for both prolate and upside-down button-mushroom-shaped drops. To account for the internal circulation effect, Helenbrook & Edwards (2002) proposed a multiplication factor, $(1-0.03\,Re^{0.65}/\mu)(2+3\,\mu)/(3+3\,\mu)$, which equals 0.9748 (or 0.9596) for $\mu = 50$ and $Re = 200$ (or 500), indicating a negligible drag-reduction effect of the internal circulation in all the cases presented here. Physically speaking, internal circulation tends to reduce drag force on the drop. Yet for most cases examined here, (3.6) appears to slightly under-estimate the value of C_D. Thus, multiplying (3.6) with the 'internal-circulation-correction' factor is not expected to offer any improvement in terms of prediction accuracy.

Figure 7, along with table 7 (as in figure 5 and table 5 but for $Re = 300$), shows that the drop behaviour observed at $Re = 200$ is qualitatively retained at higher Re. Both the prolate and oblate-like deformations at a given value of We seem to be enhanced with increasing Re (for $Re \geqslant 200$). Noteworthy here is that beyond $We = 100$ the drop shape changes very little. For example, even at $We = 500$ the computed axis ratio is $\alpha = 1.576$ with $C_D = 0.7884$, which is still quite comparable to that at $We = 100$ (i.e. 1.436 and 0.7633). Unlike the cases for $\rho = 1000$ and $\mu \geqslant 100$ where drops typically become unstable at a critical Weber number $We_c < 20$, solutions for drops with $\rho = 1000$ and $\mu = 50$ at $Re = 300$ seem to exist for very large values of We without a sign of encountering the turning point. The same situation can also be observed for $Re = 200$, 400, 500, etc.

According to the findings of Helenbrook & Edwards (2002), increasing ρ and/or decreasing μ tend to result in more pronounced prolate deformations. If μ is reduced to 40, the drops at $Re = 100$ indeed no longer deform into a shape with $\alpha > 1$ (e.g. oblate) for $We < 10$. But complicated shapes with $\alpha > 1$, such as the button mushroom shapes in figures 6 and 7, appear persistently at large values of We even at $\mu = 20$. On the other hand, if μ is increased to 70, no prolate drops can be obtained anymore for $Re \leqslant 300$. But drops at $Re = 500$ may still have $\alpha < 1$ for $We \sim 5$ until $\mu > 80$. Thus, cases with $\mu < 80$, especially when $\mu \sim 50$ (for $\rho = 1000$), present unique opportunities for steady axisymmetric liquid drops to exhibit drop shapes with both $\alpha < 1$ (such as prolate) and $\alpha > 1$ (such as oblate), and also to survive large-We conditions (at least for $Re \geqslant 100$), provided that the drop surfaces are free from surface-active contaminants. However, oblate shapes are often observed for a liquid drop moving in a gas probably because either the value of μ is large (e.g. >100)

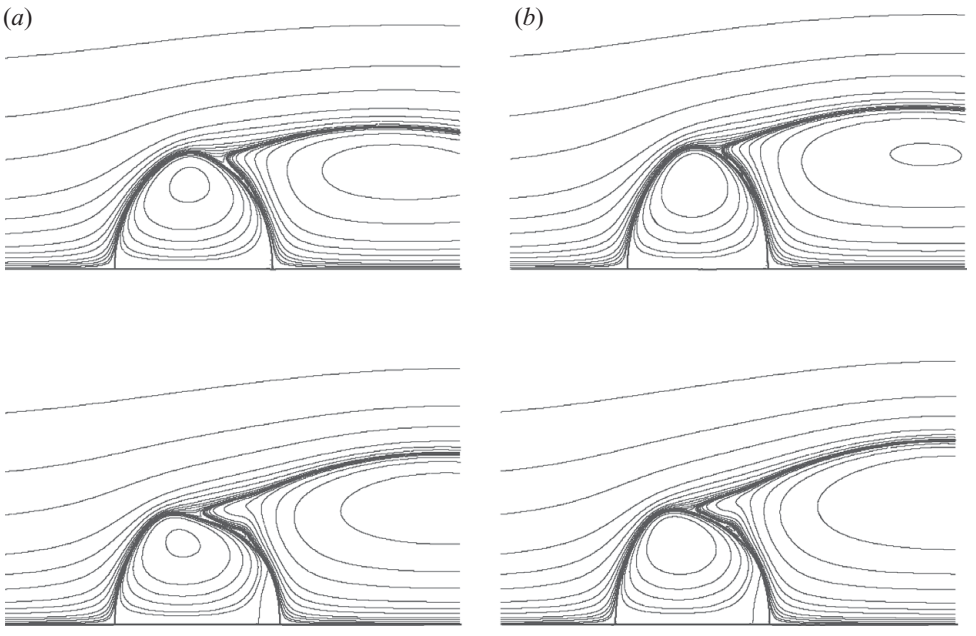

FIGURE 8. Same as figure 2 but for $We = 10$ at $Re = 200$ (top row) and 400 (bottom row), each having $(\rho, \mu) = (750, 75)$ in (a) with $\alpha = 1.474$ and 1.348, $C_D = 1.0071$ and 0.6989, and (1250, 125) in (b) with $\alpha = 1.736$ and 1.486, $C_D = 1.1149$ and 0.7327 (for fixed $\rho/\mu = 10$).

or the presence of surface-active contaminants tends to enhance the liquid viscosity effect (Haywood *et al.* 1994*a*; Helenbrook & Edwards 2002). For water drops in air, the experimentally observed internal circulation intensity seems to be somewhat less than that predicted by numerical steady solutions, which Pruppacher & Klett (1997) attributed to drop oscillations that tend to disrupt the internal circulation. The time-dependent, disruptive internal circulations in water drops (of diameter >1 mm) suspended in air were also reported in a recent wind-tunnel study of Szakáll, Diehl & Mitra (2009). Therefore, the shape of large water drops with observable deformations in air often appears to be oblate due to the expected reduction of overall internal circulation effect by the disruptive transient nature of the flow field even with $\mu \sim 50$.

3.4. *Solutions for ρ/μ or ρ/μ^2 fixed at specified values*

Multiplying Re by ρ/μ yields the Reynolds number value for the liquid flow inside the drop. Thus, it might be expected that with the value of ρ/μ fixed, the solutions would be virtually invariant. Figure 8 shows the streamlines and drop shapes at $\rho/\mu = 10$ (i.e. $\rho = 750$ and $\mu = 75$, $\rho = 1250$ and $\mu = 125$, the same as $\rho = 1000$ and $\mu = 100$) for $Re = 200$ and 400 with $We = 10$, and figure 9 those at $\rho/\mu = 5$ (i.e. $\rho = 750$ and $\mu = 150$, $\rho = 1250$ and $\mu = 250$, same as $\rho = 1000$ and $\mu = 200$).

Indeed, there is very little qualitative change in the drop shape and flow structure for a $\pm 25\,\%$ variation of ρ and μ from $\rho = 1000$, with ρ/μ fixed at a specified value, except the internal circulation intensity which is mostly determined by the value of μ. For example, the value of C_D varies within $\pm 7\,\%$ from that with $\rho = 1000$ and $\mu = 100$, and α within $\pm 10\,\%$ for cases of $\rho/\mu = 10$ in figure 8, with the drop at $Re = 400$ varying less than that at $Re = 200$. For cases of $\rho/\mu = 5$ in figure 9, C_D varies within $\pm 2\,\%$ and α within $\pm 4\,\%$. But the value of v_{ic} varies about $\pm 20\,\%$,

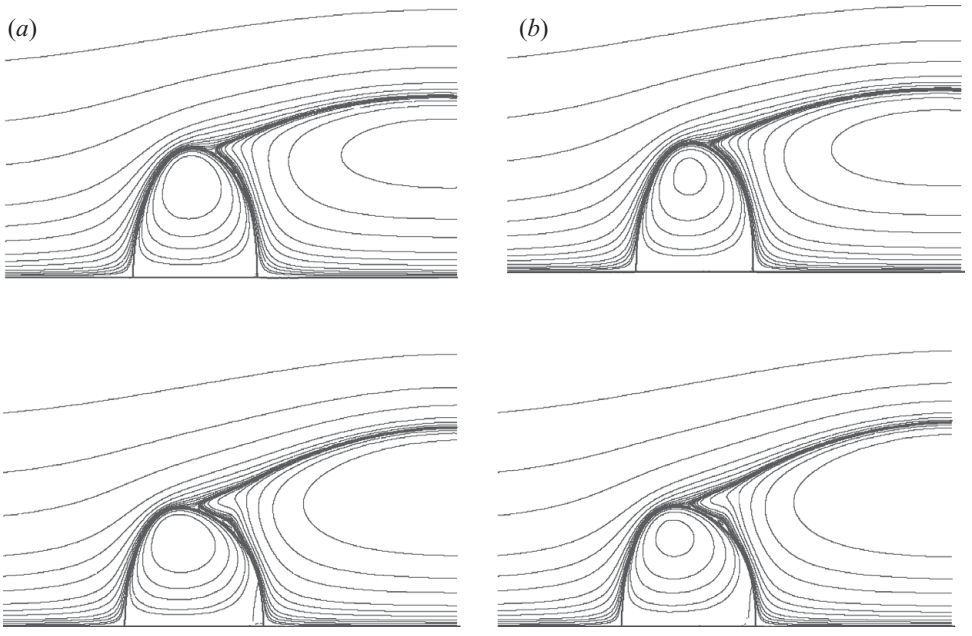

FIGURE 9. Same as figure 8 but having $(\rho, \mu) = (750, 150)$ in (a) with $\alpha = 2.082$ and 1.718, $C_D = 1.2157$ and 0.7780, and (1250, 250) in (b) with $\alpha = 2.187$ and 1.790, $C_D = 1.2411$ and 0.7925 (for fixed $\rho/\mu = 5$).

corresponding to the $\pm 25\,\%$ variation of μ. As expected, with reducing internal circulation intensity for increasing μ, C_D would vary less than $\pm 0.5\,\%$ and α within $\pm 1\,\%$ for $\rho/\mu = 2.5$ (i.e. $\rho = 750$ and $\mu = 300$, $\rho = 1250$ and $\mu = 500$, the same as $\rho = 1000$ and $\mu = 400$).

The reason for slight variations even with the value of ρ/μ fixed is that the free-surface flows are not solely determined by Re and $\rho\, Re/\mu$. Although at a fixed value of ρ/μ the values of Reynolds number for both the gas external to and the liquid internal to the drop are fixed, the value of the Weber number We inside the drop can still vary with a change of ρ (almost regardless of the value of μ), and the intensity of internal circulation can vary with a change of μ (almost regardless of the value of ρ). Dandy & Leal (1989) showed that for $Re = 100$ and $We = 4$ with $\rho \sim 1$ and $\rho/\mu = 0.25$ (as well as with other examples) 'neither the internal Reynolds number nor the density ratio plays an important role in determining the flow field'. The value of μ, which determines the intensity of internal circulation, appeared to influence the drop behaviour much more significantly than ρ.

Actually, if the value of ρ/μ^2 is fixed instead of ρ/μ, i.e. the Ohnesorge number Oh (as defined in (2.10)) is fixed instead of $\rho\, Re/\mu$, variations in C_D and α as ρ changes from 750 to 1250 become almost negligible. For example, with ρ/μ^2 fixed at 0.1 (i.e. $\rho = 750$ and $\mu = 86.6025$, $\rho = 1250$ and $\mu = 111.8034$) at $We = 10$, both C_D and α vary within $\pm 0.5\,\%$ from that with $\rho = 1000$ and $\mu = 100$ for the present results computed at $Re = 200$ ($Oh = 0.050$) and 400 ($Oh = 0.025$). Even at $\rho = 500$, $\mu = 70.7107$ and $\rho = 1500$, $\mu = 122.4745$ (i.e. $\rho/\mu^2 = 0.1$), the computed values of C_D and α are still within $\pm 2\,\%$ from that for $\rho = 1000$ and $\mu = 100$. Hence, the best choice for preserving the basic features in deforming drops while varying ρ and μ is to keep ρ/μ^2 (i.e. Oh) at a fixed value. In other words, Oh is the parameter that

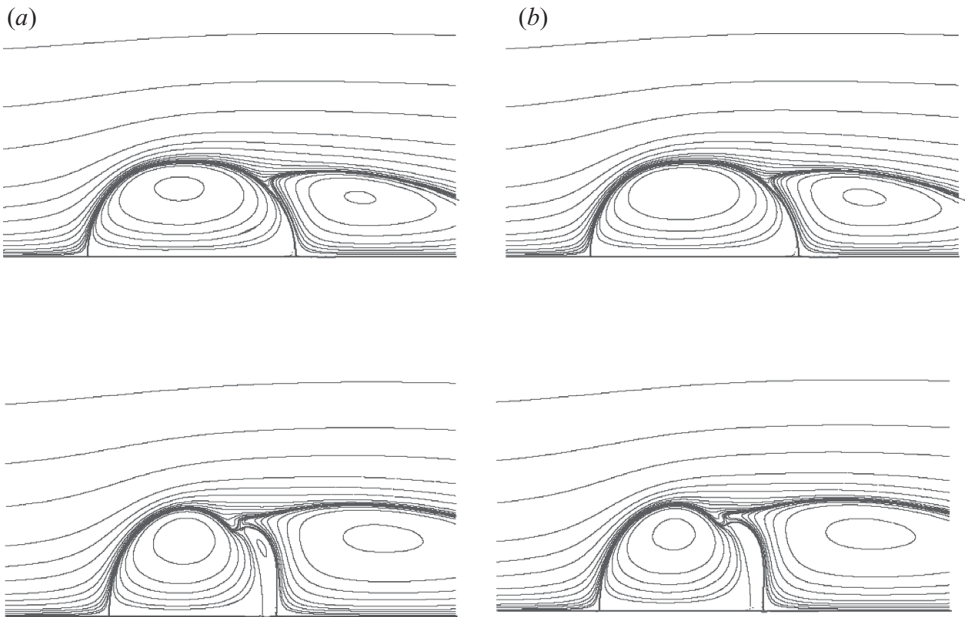

FIGURE 10. Same as figure 8 but for $Re = 200$ at $We = 5$ and 100, each having $(\rho, \mu) = (750, 43.3013)$ in (a) with $\alpha = 0.912$ and 1.291, $C_D = 0.7151$ and 0.8588, and (1250, 55.9017) in (b) with $\alpha = 0.909$ and 1.297, $C_D = 0.7171$ and 0.8632 (for fixed $\rho/\mu^2 = 0.4$).

actually controls the basic features of deforming drops at given values of Re and We. However, for $\rho/\mu^2 \leqslant 0.025$ or $\rho/\mu \leqslant 5$ the difference between fixing ρ/μ^2 and fixing ρ/μ becomes almost negligible for the result is insensitive to the ($\pm 25\,\%$) change of already large enough μ (as seen in figure 4 and table 4).

The cases at $\rho/\mu^2 = 0.4$ (i.e. $\rho = 750$ and $\mu = 43.3013$, $\rho = 1250$ and $\mu = 55.9017$, the same as $\rho = 1000$ and $\mu = 50$) are shown in figure 10 for relatively small μ with more intensified internal circulations. Except for a reduced internal circulation intensity for the drop of $\rho = 1250$ and $\mu = 55.9017$, all the other basic features such as the drop shape and external flow field appear very close to those of $\rho = 750$ and $\mu = 43.3013$ at both $We = 5$ and 100 (for $Re = 200$). Thus, the values of C_D and α do not vary more than 1 % for given values of Re and We with ρ/μ^2 fixed at 0.4 while varying ρ and μ by $\pm 25\,\%$. More intensified internal circulation (with $v_{ic} = 6.717 \times 10^{-2}$) can clearly be observed in the drop of $\rho = 750$ and $\mu = 43.3013$ at $We = 100$ with a more noticeable secondary eddy than that of $\rho = 1250$ and $\mu = 55.9017$ (with $v_{ic} = 5.213 \times 10^{-2}$). Yet the external flow fields as well as the drop shapes are almost identical for $\rho = 750$ and 1250 at given values of Re and We (as shown in figure 10 for $\rho/\mu^2 = 0.4$).

4. Discussion

Enabled by a Galerkin finite-element method with a boundary-fitted quadrilateral mesh, solutions are computed for steady axisymmetric flow internal and external to a deformable liquid drop falling through a quiescent gas. Both the flow field and free-surface profile can be determined with sufficient accuracy in great detail, for parameters relevant to the motion of liquid drops in gases. Considering the ranges of density and viscosity for common liquids and gases, most results are presented around

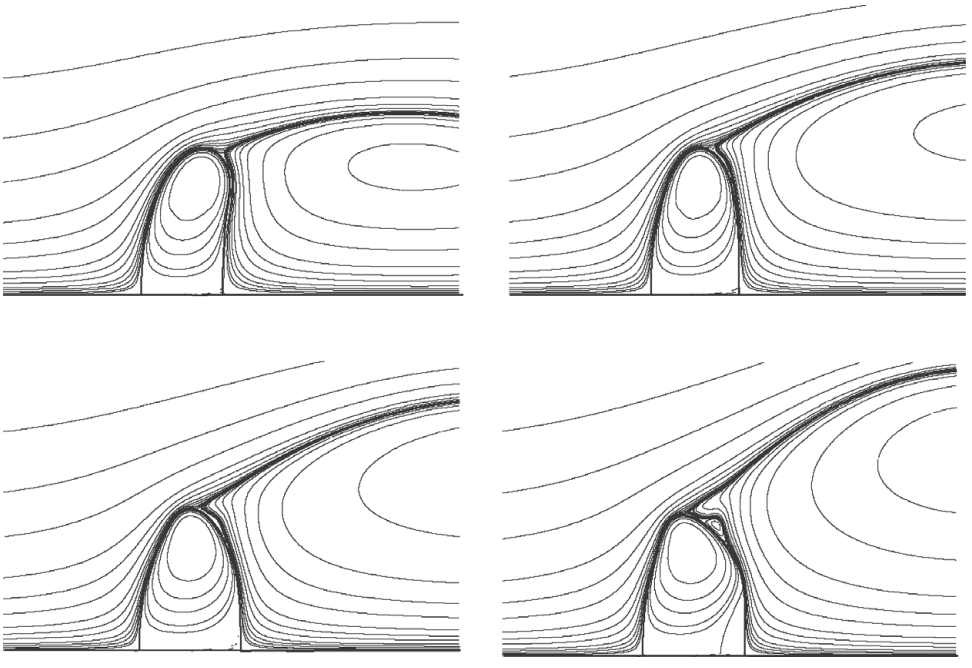

FIGURE 11. Same as figure 2 but for $Re = 100$, 200, 300 and 500 at corresponding critical Weber number We_c (= 13.521, 15.602, 17.491 and 19.591, left to right from top left to bottom right), with $\rho = 1000$ and $\mu = 100$.

the nominal cases for the liquid-to-gas density ratio $\rho = 1000$ and liquid-to-gas viscosity ratio $\mu = 100$ at the Reynolds number $100 \leqslant Re \leqslant 500$ and the Weber number $We \geqslant 1$, where drops are expected to exhibit substantial deformations. Although solutions for steady axisymmetric drops at $Re > 500$ can still be computed, they may not be realizable in the laboratory experiments because of the onset of wake eddy shedding often observed at $Re \sim 200$ (Clift *et al.* 1978). But the steady axisymmetric solutions for $Re > 200$ may still be used to reasonably describe the time-smoothed behaviour of an oscillating drop with an unsteady wake. For example, LeClair, Hamielec & Pruppacher (1970) showed that steady axisymmetric solutions could predict drag on a sphere in close agreement with experimental data up to $Re = 400$, even when the flow in the wake is realistically no longer steady and axisymmetric.

For $\rho \sim 1000$ and $\mu \sim 100$, most liquid drops moving at $Re < 300$ with $We < 1$ are rather expected to behave like rigid spheres with negligible deformations. Due to large viscosity ratio μ, the internal circulation inside the drop does not seem to have much effect on the drag force. The drop deformation becomes visually noticeable when $We \sim 5$ and is enhanced with increasing We at a given value of Re. Drops of $Re < 200$ tend to have a rounded front and flattened or even dimpled rear (referred to as 'bowl-shaped drop' by Hsiang & Faeth 1995), and those of $Re > 200$ a flattened front and somewhat rounded rear (referred to as 'dome-shaped drop' by Hsiang & Faeth 1995), with that at $Re = 200$ exhibiting an almost fore–aft symmetric shape. As an indicator of drop deformation, the axis ratio α increases with increasing We and μ, but decreases with increasing Re. The 'shape instability' at the critical Weber number We_c, corresponding to a turning point in the mathematical parameter space, typically occurs for $10 \leqslant We \leqslant 20$ where drops are severely deformed, as illustrated in figure 11. This seems to match the findings of Hsiang &

Faeth (1992, 1995) for the 'bag break-up' that typically occurs at $10 \leqslant We \leqslant 20$ for $Oh < 1$.

If ρ is fixed at 1000 and μ is varied, the drop shape can change drastically from $\alpha < 1$ (such as prolate) to $\alpha > 1$ (such as oblate) when $\mu < 80$ (with $100 \leqslant Re \leqslant 500$). For $\mu = 50$, a drop at $Re \geqslant 200$ can exhibit a prolate shape ($\alpha < 1$) when $We < 10$ and an upside-down button mushroom shape with $\alpha > 1$ when $We > 10$ (as shown in figures 6 and 7). However, as commented by Helenbrook & Edwards (2002), prolate drops are expected to be axisymmetrically unstable because a falling object tends to align with the long axis normal to the flow; this might be the reason why prolate falling drops have never been reported. For $\mu \geqslant 100$ with increasing We, drops at $Re \geqslant 100$ always deform into more and more oblate-like shapes with $\alpha > 1$. The drop shape and external flow structure become rather insensitive to the value of μ for $\mu \geqslant 200$, when the (dimensionless) internal circulation intensity v_{ic} – the maximum internal circulation velocity – is below ~ 0.025.

Interestingly, the fitted formula of Clift *et al.* (1978) for the observed axis ratio of liquid drops falling in air as a function of the Eötvös number Eo, i.e. (3.5), seems to describe the axis ratio of computed drops quite well for the case of $\rho = 1000$ and $\mu = 200$, but not as well at other values of μ. For the drag coefficient C_D though, a straightforward modification of the formula recommended by Clift *et al.* (1978) for rigid spheres by replacing the radius of the sphere with the radius of the cross-sectional area, as in (3.6), is found to be quite accurate when compared with the computed values of C_D for all the cases considered here. If the drop shape is assumed to be reasonably represented as an ellipsoid with $r_{max} = \alpha^{1/3}$ (as in Helenbrook & Edwards 2002), (3.6) can also be written as

$$Eo = 18\,\alpha^{1/3}\,Ca\,\left[1 + 0.1935\,(\alpha^{1/3}\,Re)^{0.6305}\right], \tag{4.1}$$

which is an implicit equation for α. Indicated by (4.1) is the fact that the value of α also depends on Ca and Re besides Eo. Therefore, it is not surprising to find that (3.5) has only limited predictability. Actually using $\alpha^{1/3}$ to estimate r_{max} appears to be quite reasonable for most of the cases computed here. For example, in table 3 at $Re = 100$, 200 and 500 the corresponding values of $\alpha^{1/3}$ are 1.176, 1.109 and 1.250, which are quite comparable to 1.193, 1.101 and 1.248, the values of r_{max}, respectively. Even for the drops in table 4 with enhanced deformations at $\mu = 1000$ and $Re = 100$, the value of $\alpha^{1/3}$ is 1.399 (versus $r_{max} = 1.348$). But for the drops in figures 6 and 7 with button mushroom shapes being too far from an ellipsoidal shape, the value of $\alpha^{1/3}$ can no longer be used to approximate the radius of cross-sectional area r_{max}.

The computed results for various Re and We at $\rho = 1000$ and different values of μ are shown to be almost identical to the corresponding cases at $\rho = 500$ and 1500 (except for v_{ic}) as long as the value of ρ/μ^2 remains fixed. Hence, only three independent parameters such as Re, We and Oh (or ρ/μ^2), instead of four (i.e. Re, We, ρ and μ), are needed for specifying a mathematical problem to determine the drop deformation (such as α) and external flow field (such as C_D), for liquid drops moving in gases (with large ρ and μ). However, a specific value of μ is needed for determining the internal circulation intensity, if it is of particular interest. Actually the mode of drop deformation (at large values of Re) should be a result of the difference between the dynamic pressure distributions (arising from the flow convection) internal and external to the drop. According to an estimate by Helenbrook & Edwards (2002), the ratio of dynamic pressure magnitudes internal and external to the drop is expected to be proportional to ρ/μ^2. Thus, the mode of drop deformation

varies most significantly when $\rho/\mu^2 > 0.15$ (e.g. $\rho \sim 1000$ and $\mu < 80$) for liquid drops moving in gases. Because the internal circulation in a liquid drop moving in gas (roughly $\propto U/\mu$) does not have substantial intensity, its influence on the drag force may be negligible (when *We* is small). However, at large values of *We* the internal circulation can have quite significant effects on drop deformation, which tend to alter the drag force for the change of cross-sectional area, as indicated by (3.6). Thus, the internal circulation effect on drag force must be realized through its influence on drop deformation rather than reducing the viscous shear stresses along the drop surface.

It is noteworthy that the shapes of the drops in figure 4 for $\mu \geqslant 200$, especially at $Re \geqslant 300$, look very similar to those of the large water drops shown by Pruppacher & Beard (1970) through their wind-tunnel experiments. In a general description of liquid drops in air, Clift *et al.* (1978) also stated that 'the shapes of liquid drops falling through air can be conveniently represented by two oblate semispheroids with a common major semi-axis a and minor semi-axes b_1 and b_2'. Yet not all liquid drops satisfy the viscosity ratio $\mu \geqslant 200$. For example, water drops in air typically have $\mu \sim 55$ (with $\rho \sim 830$, e.g. under standard condition at 20°C and 1 atm). According to the present computational results, water drops falling through air should exhibit prolate shapes unlike those with $\rho/\mu^2 \leqslant 0.025$ (e.g. $\rho \sim 1000$ and $\mu \geqslant 200$).

The problem here might come from the assumption of steady axisymmetric flow, which may only be strictly accurate for $Re \leqslant 200$ (Clift *et al.* 1978). Significant vortex shedding effects on water drops, as indicated by a spiral falling trajectory (also known as the path instability), are typically observed when $Re > 300$. Beyond $Re \sim 300$, numerical solutions of steady axisymmetric flows could become less relevant to reality. However, LeClair *et al.* (1970) showed that steady axisymmetric solutions could predict drag on a sphere in close agreement with experimental data up to $Re = 400$, indicating that they may reasonably describe the time-smoothed behaviour of the intrinsically transient flow beyond $Re = 200$. Not surprisingly, Pruppacher & Klett (1997) suggested a cutoff point of $Re \sim 400$ for using the steady axisymmetric solutions to describe water drops falling in air. But water drops at $Re < 400$ barely deform from the spherical shape (as indicated by the computed data in table 1 as well as the drop images of Pruppacher & Beard (1970)); all noticeably deformed water drops are at $Re > 500$ where the flow in the wake becomes time-dependent, which can also cause the drop to oscillate (Beard, Ochs & Kubesh 1989) or to cant (Saylor & Jones 2005). The transient vortex shedding and associated drop oscillations tend to disrupt the internal circulation inside the liquid drop, resulting in an overall reduction of the internal circulation intensity (Pruppacher & Klett 1997; Szakáll *et al.* 2009). A similar effect of reducing the internal circulation intensity can also be obtained by simply increasing the viscosity ratio μ in a steady axisymmetric model, without computing the complicated transient, full three-dimensional flow field. Therefore, the drop shapes shown in figure 4 for $Re \geqslant 300$ and $\rho/\mu^2 \leqslant 0.025$ appear to represent the most commonly observed shapes of significantly deformed liquid drops falling in air.

The author would like to thank Professor K. Beard for bringing the drop deformation problem to his attention, as well as Dr M. Szakáll and Dr S. Mitra at the University of Mainz for stimulating discussions in their wind tunnel laboratory. The constructive comments from reviewers helped enhance the presentation and are therefore appreciated.

REFERENCES

Batchelor, G. K. 1967 *An Introduction to Fluid Dynamics*. Cambridge University Press.

Beard, K. V., Ochs III, H. T. & Kubesh, R. J. 1989 Natural oscillations of small raindrops. *Nature* **342**, 408–410.

Bozzi, L. A., Feng, J. Q., Scott, T. C. & Pearlstein, A. J. 1997 Steady axisymmetric motion of deformable drops falling or rising through a homoviscous fluid in a tube at intermediate Reynolds number. *J. Fluid Mech.* **336**, 1–32.

Brignell, A. S. 1973 The deformation of a liquid drop at small Reynolds number. *Q. J. Mech. Appl. Maths* **26**, 99–107.

Christodoulou, K. N. & Scriven, L. E. 1992 Discretization of free surface flows and other moving boundary problems. *J. Comput. Phys.* **99**, 39–55.

Clift, R. C., Grace, J. R. & Weber, M. E. 1978 *Bubbles, Drops and Particles*. Academic.

Dandy, D. S. & Leal, L. G. 1989 Buoyancy-driven motion of a deformable drop through a quiescent liquid at intermediate Reynolds numbers. *J. Fluid Mech.* **208**, 161–192.

Feng, J. Q. 2000 Contact behavior of spherical elastic particles: a computational study of particle adhesion and deformation. *Colloids Surf.* A **172**, 175–198.

Feng, J. Q. 2007 A spherical-cap bubble moving at terminal velocity in a viscous liquid. *J. Fluid Mech.* **579**, 347–371.

Feng, J. Q. & Scott, T. C. 1996 A computational analysis of electrohydrodynamics of a leaky dielectric drop in an electric field. *J. Fluid Mech.* **311**, 289–326.

Fornberg, B. 1988 Steady viscous flow past a sphere at high Reynolds numbers. *J. Fluid Mech.* **190**, 471–489.

Haberman, W. L. & Sayre, R. M. 1958 Motion of rigid and fluid spheres in stationary and moving liquids inside cylindrical tubes. *David Taylor Model Basin Rep.* 1143. U.S. Navy Dept., Washington, D.C., 1958.

Harper, J. F. 1972 The motion of bubbles and drops through liquids. *Adv. Appl. Mech.* **12**, 59–129.

Hase, M. & Weigand, B. 2004 Transient heat transfer of deforming droplets at high Reynolds number. *Intl J. Numer. Methods Heat Fluid Flow* **14** (1), 85–97.

Haywood, R. J., Renksizbulut, M. & Raithby, G. D. 1994*a* Numerical solution of deforming evaporating droplets at intermediate Reynolds numbers. *Numer. Heat Transfer* **26**, 253–272.

Haywood, R. J., Renksizbulut, M. & Raithby, G. D. 1994*b* Transient deformation and evaporation of droplets at intermediate Reynolds numbers. *Intl J. Heat Mass Transfer* **37** (4), 1401–1409.

Helenbrook, B. T. & Edwards, C. F. 2002 Quasi-steady deformation and drag of uncontaminated liquid drops. *Intl J. Multiphase Flow* **28**, 1631–1657.

Hood, P. 1976 Frontal solution program for unsymmetric matrices. *Intl J. Numer. Methods Engng* **10**, 379–399. [See *ibid.* **11**, 1055 (1977) for corrigendum.]

Hsiang, L. P. & Faeth, G. M. 1992 Near-limit drop deformation and secondary breakup. *Intl J. Multiphase Flow* **18** (5), 635–652.

Hsiang, L. P. & Faeth, G. M. 1995 Drop deformation and breakup due to shock wave and steady disturbance. *Intl J. Multiphase Flow* **21** (4), 545–560.

Kistler, S. F. & Scriven, L. E. 1983 Coating flows. In *Computational Analysis of Polymer Processing* (ed. J. R. A. Pearson & S. M. Richardson), pp. 243–299. Applied Science.

LeClair, B. P., Hamielec, A. E. & Pruppacher, H. R. 1970 A numerical study of the drag on a sphere at low and intermediate Reynolds numbers. *J. Atmos. Sci.* **27** (2), 308–315.

LeClair, B. P., Hamielec, A. E., Pruppacher, H. R. & Hall, W. D. 1972 Theoretical and experimental study of the internal circulation in water drops falling at terminal velocity in air. *J. Atmos. Sci.* **29**, 728–740.

Miller, C. A. & Scriven, L. E. 1968 The oscillations of a fluid droplet immersed in another fluid. *J. Fluid Mech.* **32**, 417–435.

Ortega, J. M. & Rheinoldt, W. C. 1970 *Iterative Solution of Nonlinear Equations in Several Variables*. Academic.

Pruppacher, H. R. & Beard, K. V. 1970 A wind tunnel investigation of the internal circulation and shape of water drops falling at terminal velocity in air. *Q. J. R. Meteorol. Soc.* **96**, 247–256.

Pruppacher, H. R. & Klett, J. D. 1997 *Microphysics of Clouds and Precipitation*, 2nd edn. Kluwer.

Ryskin, G. & Leal, L. G. 1984 Numerical solution of free-boundary problems in fluid mechanics. Part 2. Buoyancy-driven motion of a gas bubble through a quiescent liquid. *J. Fluid Mech.* **148**, 19–35.

de Santos, J. M. 1991 Two-phase cocurrent downflow through constricted passages. PhD thesis, University of Minnesota.

Saylor, J. R. & Jones, B. K. 2005 The existence of vortices in the wakes of simulated raindrops. *Phys. Fluids* **17**, 031706.

Strang, G. & Fix, G. J. 1973 *An Analysis of the Finite Element Method*. Prentice-Hall.

Szakáll, M., Diehl, K. & Mitra, S. K. 2009 A wind tunnel study on shape, oscillation, and internal circulation of large raindrops with sizes between 2.5 and 7.5 mm. *J. Atmos. Sci.* **66**, 755–765.

Taylor, G. I. 1964 Disintegration of water drops in an electric field. *Proc. R. Soc. Lond.* A **280**, 383–397.

Taylor, T. D. & Acrivos, A. 1964 On the deformation and drag of a falling viscous drop at low Reynolds number. *J. Fluid Mech.* **18**, 166–176.

Tryggvason, G., Bunner, B., Esmaeeli, A., Juric, D., Al-Rawahi, N., Tauber, W., Han, J., Nas, S. & Jan, Y.-J. 2001 A frontal tracking method for the computations of multiphase flow. *J. Comput. Phys.* **169**, 708–759.

Yang, B. & Prosperetti, A. 2007 Linear stability of the flow past a spheroidal bubble. *J. Fluid Mech.* **582**, 53–78.